

# JGR Space Physics

## RESEARCH ARTICLE

10.1029/2025JA034569

### Key Points:

- Correlation function analysis of high-resolution data over short time intervals reveals ion scale turbulence at ( $\sim 100$ – $1,000$  km) scales
- Fluctuations parallel to the magnetic field have shorter correlation lengths than transverse ones, showing stronger compressive dissipation
- Transverse correlation functions vary roughly as the inverse sine of the cone angle, showing dominant 2D turbulence

### Correspondence to:

A. J. G. Angeles,  
[alvin.angeles@unh.edu](mailto:alvin.angeles@unh.edu)



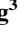
### Citation:

Angeles, A. J. G., Spence, H. E., Smith, C. W., Vasquez, B. J., Cohen, I. J., Genestreti, K. J., et al. (2025). The correlation function for magnetic field fluctuations at ion dissipation scales in the solar wind. *Journal of Geophysical Research: Space Physics*, 130, e2025JA034569. <https://doi.org/10.1029/2025JA034569>

Received 15 AUG 2025

Accepted 7 DEC 2025

## The Correlation Function for Magnetic Field Fluctuations at Ion Dissipation Scales in the Solar Wind

Alvin J. G. Angeles<sup>1</sup> , Harlan E. Spence<sup>1</sup> , Charles W. Smith<sup>1</sup> , Bernard J. Vasquez<sup>1</sup> , Ian J. Cohen<sup>2</sup> , Kevin J. Genestreti<sup>1</sup> , Ruth Skoug<sup>3</sup> , Savvas Raptis<sup>2</sup> , Christine Gabrielse<sup>4</sup> , Daniel J. Gershman<sup>5</sup> , David Fischer<sup>6</sup> , Christopher T. Russell<sup>7</sup> , James L. Burch<sup>8</sup> , Roy B. Torbert<sup>1</sup> , and Werner Magnes<sup>6</sup> 

<sup>1</sup>Department of Physics and Astronomy, Institute for the Study of Earth, Oceans, and Space, University of New Hampshire, Durham, NH, USA, <sup>2</sup>Applied Physics Laboratory, John Hopkins University, Laurel, MD, USA, <sup>3</sup>Los Alamos National Laboratory, Los Alamos, NM, USA, <sup>4</sup>The Aerospace Corporation, Chantilly, VA, USA, <sup>5</sup>NASA Goddard Space Flight Center, Greenbelt, MD, USA, <sup>6</sup>Space Research Institute, Austrian Academy of Science, Wien, Austria, <sup>7</sup>Institute of Geophysics and Planetary Physics, University of California, Los Angeles, CA, USA, <sup>8</sup>Southwest Research Institute, San Antonio, TX, USA

**Abstract** This study investigates energy dissipation in small-scale solar wind turbulence using a novel approach to autocorrelation function analysis leveraging high-resolution data from the Magnetospheric Multiscale Mission (MMS). We analyze magnetic field fluctuations at ion dissipation scales, focusing on short 20-s intervals to isolate dissipation-scale dynamics. Using MMS's fluxgate magnetometer, fast plasma investigation, and energetic particle detector, we compute normalized correlation functions as functions of the interplanetary magnetic field cone angle. Our results show that turbulence is correlated over short spatial scales ( $\sim 100$ – $1,000$  km), with shorter correlation lengths in the compressional component compared to the transverse components. We find that the transverse correlation lengths differ most when the interplanetary magnetic field is nearly perpendicular to the solar wind flow (cone angle  $\sim 90^\circ$ ), and that they vary approximately as the inverse sine of the cone angle. The characteristics of the correlation length suggest that the turbulence observed is primarily two-dimensional. These findings highlight the anisotropic nature of dissipation-scale turbulence and its dependence on solar wind conditions, providing insights into energy transfer in space plasmas.

**Plain Language Summary** In this study, we use data from the NASA Magnetospheric Multiscale Mission (MMS) to explore how turbulence in the solar wind behaves. Solar wind turbulence is often characterized as the chaotic evolution of plasma from the Sun. Turbulence in the solar wind is classified into three regimes that differentiate, among other things, the size of the fluctuations. In this investigation, we are interested in how turbulence behaves at the smallest scales where the fluctuations are small enough to interact with suprathermal particles. Using the detectors onboard MMS, we are able to extract different parameters of the solar wind, including the solar magnetic field and particle velocity. Our findings demonstrate that turbulence in the solar wind at these small scales has variable behaviors that can provide future studies with the groundwork for further understanding of the nature of turbulence.

## 1. Introduction

Solar wind turbulence is a complex nonlinear phenomenon that exhibits strong anisotropy with respect to the mean magnetic field, manifesting in direction dependent fluctuations and cascade dynamics across multiple scales which resemble the behavior of classic hydrodynamic turbulence (Goldstein et al., 1995; Matthaeus & Goldstein, 1982). Two theoretical frameworks dominate its study: interacting linearized waves (e.g., Alfvén waves; (Coleman, 1966)) and magnetohydrodynamics (MHD) turbulence studied as an extension of hydrodynamic turbulence (Goldstein et al., 1995; Matthaeus & Goldstein, 1982; Peebles, 1968). Magnetic field measurements of space plasmas at ion scales are often categorized into three regions. These regions are known as the energy containing range, inertial range, and dissipation range, see Smith and Vasquez (2021) for a review.

There are two forms of anisotropy often discussed in studies of solar wind turbulence: the anisotropy of the fluctuation and the anisotropy of the underlying wave vector. The magnetic fluctuation vector is generally seen to be perpendicular to the mean magnetic field with smaller fluctuations associated with compression (Belcher & Davis, 1971). At large inertial range scales, turbulence exhibits a wave vector anisotropy relative to the mean

magnetic field, often visualized as a “Maltese Cross” in two-dimensional correlation functions (Matthaeus et al., 1990). Subsequent study of the same range found that wave vector anisotropy of solar wind fluctuations is dependent on solar wind speed—with fast streams dominated by quasi-parallel wave vectors, whereas slow streams are dominated by quasi-perpendicular ones (Dasso et al., 2005). However, less is known about turbulence at dissipation scales, where energy is converted to heat (Leamon et al., 1998, 1999; Smith et al., 2006), and the nature of small-scale structure (Smith et al., 2013) particularly at electron scales. This study addresses the dissipation range directly by applying a modified correlation function analysis to high-time-resolution MMS data, enabling the investigation of magnetic field fluctuations at ion scales by focusing on short time intervals to isolate dissipation-scale dynamics.

The energy range, associated with spacecraft frame frequencies (frequencies measured in the spacecraft's reference frame)  $f < 10^{-4}$  Hz at 1 AU (Matthaeus et al., 1994; Smith & Vasquez, 2021) reflect the large scale structures that originate from the Sun (Davis et al., 2023; Magyar & Doorsselaere, 2022; Matthaeus & Goldstein, 1986; Smith & Vasquez, 2024). This range acts as a stockpile of energy that is injected into turbulence by nonlinear dynamics that cascades down into smaller scales and drives their respective fluctuations.

The magnetic spectrum in the inertial range is typically observed in a frequency ranging from  $[10^{-4}–10^{-1}]$  Hz at 1 AU (Alexandrova et al., 2013). In the interplanetary medium, the inertial range is the most widely studied region of the magnetic spectrum. Here, both magnetic field and velocity fluctuations exhibit power law behavior resembling that of hydrodynamic turbulence (Alexandrova et al., 2013; Podesta et al., 2006; Smith & Vasquez, 2021). In this range, energy is approximately conserved as it cascades from larger to smaller scales without significant dissipation. Due to the presence of local mean magnetic fields, turbulent isotropy breaks down leading to an anisotropic quasi 2D state (Matthaeus et al., 1990). Both MHD and kinetic simulations confirm that the turbulent cascade is strongest in directions perpendicular to the mean magnetic field in the inertial range (Cho & Vishniac, 2000; Matthaeus et al., 1996, 1998; Oughton et al., 1994; Shebalin et al., 1983; Vasquez et al., 2014). Observations at 1 AU concur with the simulations and indicate that two-dimensional (2D) turbulence—turbulent fluctuations where the wave vectors are primarily perpendicular to the mean field—dominate slab turbulence, which are turbulent fluctuations where the wave vectors are primarily parallel to the mean field (Bieber et al., 1996; Hamilton et al., 2008; Smith et al., 2012).

The dissipation range, where turbulent energy is converted into thermal energy, occurs at ion kinetic scales and is typically observed at frequencies of a few tenths of a Hz in the spacecraft reference frame at 1 AU. Extensive solar wind studies at 1 AU reveal that this range typically occurs at  $\sim 0.3$  Hz (Leamon et al., 1998, 1999; Smith et al., 2006) at scales relating to the Larmor radius of thermal protons and the proton inertial scale. Further decomposing the scale, the ion dissipation range is thought to be  $\sim [0.1–1]$  Hz (Alexandrova et al., 2013) and electron dynamics tend to dominate from  $\sim [1–100]$  Hz. Previous surveys with the Cluster spacecraft had concluded that a high signal-to-noise ratio was needed to fully characterize the turbulent cascade and dissipation at the electron scale in addition to high time resolution of ion and electron distributions (Sahraoui et al., 2013).

Despite significant advances in understanding inertial-range turbulence, dissipation-scale processes such as cyclotron damping, Landau damping, and current sheet formation (Barnes, 1966; Bourouaine & Chandran, 2013; Bowen et al., 2024; Dmitruk et al., 2004; Hollweg & Isenberg, 2002; Isenberg & Vasquez, 2015; Markovskii & Vasquez, 2011; TenBarge et al., 2013; Vasquez, 2015; Yang et al., 2017) remain less explored due to the need for high-resolution data and short time intervals. In this study, we address this gap by analyzing ion-scale magnetic field fluctuations in the pristine solar wind using MMS data. Employing a modified correlation function analysis in a mean-field aligned coordinate system, we demonstrate that dissipation-scale turbulence is highly anisotropic; correlation lengths are consistently shorter along the direction parallel to the mean magnetic field than in the perpendicular directions. In addition, we find correlation length anisotropy within the same mean-field coordinates used by Belcher and Davis (1971) at large angles. These findings are consistent with MHD and kinetic simulations showing that the turbulent cascade is strongest in the perpendicular directions to the mean magnetic field (Cho & Vishniac, 2000; Matthaeus et al., 1996, 1998; Oughton et al., 1994; Shebalin et al., 1983; Vasquez et al., 2014), as well as with observations indicating the prevalence of the two-dimensional component over slab turbulence at 1 AU (Bieber et al., 1996; Hamilton et al., 2008; Smith et al., 2012). Furthermore when analyzing turbulence in different cone angles—defined as the angle between the interplanetary magnetic field (IMF) and the solar wind direction—we find (a) that the correlation lengths of the correlation function components transverse to the mean magnetic field,  $X$  and  $Y$ , differ most at  $\sim 90^\circ$ , where the magnetic field is nearly perpendicular to the

flow, and (b) that the  $X$  and  $Y$  correlation lengths vary approximately as the inverse sine of the cone angle. These two properties of the correlation length suggest that the turbulence examined here is predominately 2D. This study reveals the anisotropic nature of dissipation-scale turbulence and its dependence on solar wind parameters, offering new insights into energy dissipation in space plasmas.

In Section 2, we describe the MMS spacecraft (Burch et al., 2016), data selection, coordinate system, and correlation function methodology. Section 3 presents the results of the correlation and second-order structure function analysis, including their dependence on cone angles and energetic particles. In Section 4, we interpret our findings in the context of other studies. Finally, Section 5 summarizes our conclusions and provides directions for future work.

## 2. Methodology

We analyzed solar wind turbulence at dissipation scales using MMS-1 data from 21 February 2019, focusing on short (20-s) intervals to isolate small-scale fluctuations. Our approach involved: (a) selecting high-resolution data from MMS instruments, (b) transforming magnetic field data into Field-Aligned Coordinates (FAC), and (c) computing normalized autocorrelation and structure functions to determine correlation lengths. Below, we detail each step.

### 2.1. Instrument

To achieve the high resolution needed for ion dissipation range analysis, we used MMS-1's fluxgate magnetometer (FGM, 16 samples/second) (Russell et al., 2016; Torbert et al., 2016) and fast plasma investigation (FPI) (Pollock et al., 2016). In addition, we utilized the MMS Energetic Ion Spectrometer (EIS), part of the Energetic Particle Detector (EPD) suite to observe protons over the energy range [20 keV – > 0.5 MeV] (Mauk et al., 2016). Spacecraft position was determined using the Magnetic Ephemeris Coordinates (MEC) (Tooley et al., 2016) system.

The FPI on MMS-1 includes the Dual Ion Spectrometer (DIS) and Dual Electron Spectrometer (DES) used to measure ion and electron distributions, respectively. Data taken from these instruments were taken from the fast mode survey which has a resolution of 4.5 s, and is comprised of an aggregate of data taken at burst mode which has a resolution of 30 (electrons) to 50 ms (ions) (Gershman et al., 2022). The FGM data products consists of an analog fluxgate magnetometer (AFG) and a digital fluxgate magnetometer (DFG). Data from the AFG were taken on fast survey mode which takes at 16 samples per second (Russell et al., 2022).

### 2.2. Data Selection

The geometry of solar wind turbulence is often described using two-dimensional correlation functions, which reveal anisotropy relative to the mean magnetic field (Matthaeus et al., 1990). Large-scale fluctuations exhibit a “Maltese Cross” pattern, with fast and slow wind regimes showing distinct anisotropies — quasi-parallel in fast and quasi-perpendicular in slow (Dasso et al., 2005).

While these earlier studies focused on inertial scales, our analysis extends into the dissipation range. We achieve higher data resolution by utilizing shorter time intervals on the order of minutes and seconds to resolve the spatial structure of fluctuations within the dissipation range without the resulting behavior being dominated by the energy contained at larger scales. This approach allows us to convert the lower frequency fluctuations of the field into contributions to the local mean field, removing the low frequency power from the calculation of the correlation length. This enables the exploration of correlation length scales associated with these small scale fluctuations and their averaged effects over a large summation of short time intervals.

Utilizing the Python Space Physics Data Analysis Software (PySPEDAS), we downloaded the data sets from the MMS Data Science Center. Data was obtained from MMS-1 for 21 February 2019, 04:00:00–11:30:00 UTC, during a solar wind turbulence campaign providing uninterrupted high-resolution measurements.

To avoid fluctuations due to kinetic instabilities such as cyclotron resonant instabilities associated with super-thermal ions and electrons that originate at the bow shock or within the magnetosphere we wanted to ensure that the in situ data gathered by MMS originated in the ambient solar wind upstream of the magnetopause and as much as possible given the mission's orbital limitations, outside the ion and electron foreshock regions. Figure 1 and Table 1

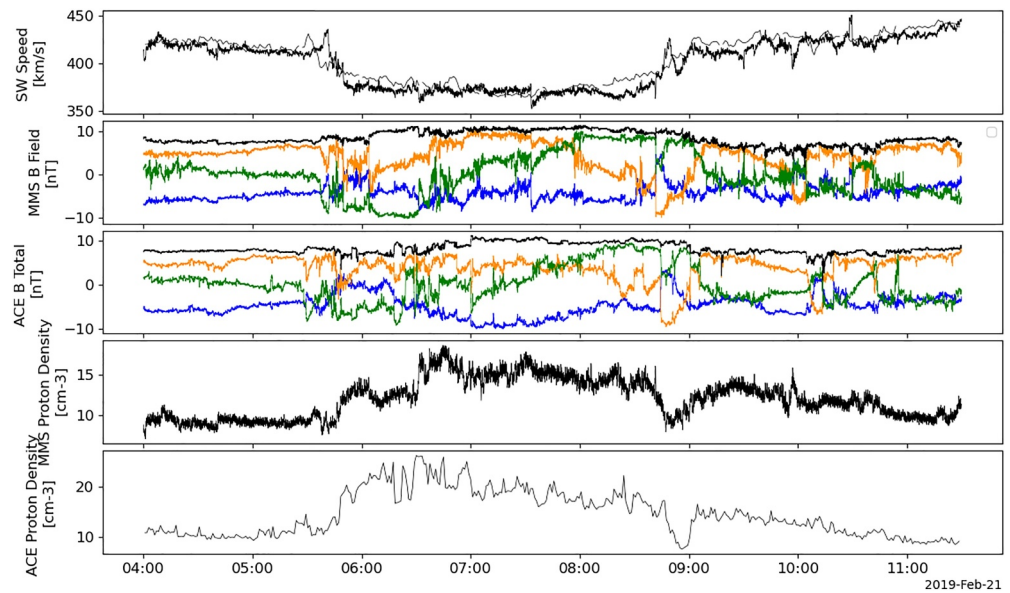


**Figure 1.** Solar wind parameters on 21 February 2019, 04:00:00–11:30:00 UTC, from MMS-1 (dark lines) and ACE (light lines, propagated from L1 to 1 AU). Top: Ion speed (km/s). Middle: Magnetic field strength (nT) in GSE (X: blue, Y: orange, Z: green, total: black). Bottom: Solar wind proton density ( $\text{cm}^{-3}$ ). Comparison confirms measurements are in the pristine solar wind.

display several properties of the solar wind plasma during this time interval, with the majority of average values in Table 1 falling within the nominal range expected in the solar wind (Barnes, 1979; Verscharen et al., 2019).

Given MMS's relative proximity to Earth ( $\sim 25 R_E$ ), we verified that measurements reflect pristine solar wind by comparing with ACE data at L1. To accomplish this, we leveraged data from the Advanced Composition Explorer (ACE) mission, which is positioned upstream of Earth at the L1 point. Using the average solar wind speed from MMS as shown in Table 1, we estimated the propagation delay from 1 AU (where MMS is located) to the L1 point where ACE is situated. Based on the average distance between Earth and L1, along with the mean solar wind speed ( $\sim 400 \text{ km s}^{-1}$ ; see Table 1) during the analyzed 7.5 hr interval, we estimated a propagation delay of approximately 1 hr between L1 and 1 AU. Accordingly, we time shifted observations from ACE from 03:00–10:30 UTC to align with MMS observations at 04:00–11:30 UTC. Doing so allowed for a comparison of the solar wind speed, magnetic field structure, and ion density of the solar wind at both locations. However, because of the complexities of solar wind propagation, this simple speed-based propagation was not intended to be exact — the two spacecraft probably did not observe the same solar wind stream.

**Table 1**

Average Solar Wind Parameters (21 February 2019, 04:00:00–11:30:00 UTC)

Parameter	Value
Mean Magnetic Field (GSE)	8.5 nT
Mean Ion Density	$12 \text{ cm}^{-3}$
Mean Electron Density	$12.4 \text{ cm}^{-3}$
Mean Ion Speed	398.7 km/s
Mean Electron Temperature	$T_e = 11.2 \text{ eV}$
Mean Ion Temperature	$T_i = 43.4 \text{ eV}$
Mean Ion Gyroradius	$\rho_i = 112 \text{ km}$
Mean Ion Inertial Length	$d_i = 65.8 \text{ km}$
Mean Thermal Speed	$v_{th} = 9.12 \times 10^1 \text{ km/s}$

The top plot of Figure 1 shows the solar wind ion speed as recorded by the MMS and ACE spacecraft, the darker line representing MMS and the lighter one ACE. The solar wind is mostly slow and Alfvénic;  $V \leq 400 \text{ km/s}$  (Abbo et al., 2016; D'Amicis & Bruno, 2015; Dasso et al., 2005; Duan et al., 2020; Kilpua et al., 2016; Marsch et al., 1981) with no signatures of coronal mass ejection activity present observed during this interval. The second and third plots show the associated magnetic field in GSE coordinates from MMS and ACE respectively. In GSE, the Earth is at the origin, the X-axis points from Earth to the Sun, the Z-axis is aligned on the north pole of Earth's orbital plane and the Y-axis lies on the ecliptic and points in the opposite direction of Earth's orbital motion around the Sun. In these plots, blue represents the X component, orange the Y component, green the Z component, and black the total magnetic field.

When comparing solar wind speeds at L1 and 1 AU, we observe few discrepancies. Similarly, when comparing magnetic fields, there are not any

major structures visible in the MMS plot that are absent in the ACE plot. We observe a slight decrease ( $\sim 10\%$ ) in ion density from ACE to MMS. Unlike ACE, which was designed to observe the solar wind, MMS was only recently optimized for such observations in 2017. During fast survey mode intervals, the FPI instrument onboard MMS has been shown to observe lower ion densities than those observed by OMNI (Roberts et al., 2021). This discrepancy may help explain the slight difference in measured ion densities. This gives us confidence that the data within the chosen time frame are fairly representative of pristine solar wind conditions, mostly free from bow shock connection.

To further illustrate MMS-1's location in relation to the Earth and the bow shock, we utilized 3DView, a web tool designed by the French Plasma Physics Data Center (Génot et al., 2018). The top panel of Figure 2 shows the location of MMS-1 in relation to Earth and the Fairfield bow shock model (Fairfield, 1971) looking at the XY GSE plane. The bottom panel shows MMS-1 in relation to the Earth and bow shock in the ZY GSE plane. This snapshot was taken at 11:30:00 when MMS-1 was closest to the bow shock — approximately  $28.2 R_E$ . Given that this study was conducted on a geomagnetically quiet day, the Fairfield model is applicable and shows that MMS-1 was outside the bow shock.

During the course of the study, it was found that surveys conducted with the FGM instrument contained an intrinsic noise floor that contaminates frequencies  $f \geq 0.5$  Hz. To overcome this limitation, we selected intervals of data where the power spectrum was high enough to dominate the noise.

### 2.3. Coordinate Transformation

In order to avoid including excess low frequency power from the spectra at the small scales that interest us, we split the data set into 20-s intervals that each contain an equal number of data points. We selected 20-s intervals as they are short enough to resolve dissipation scales while still providing sufficient data for statistical robustness. If the total number of data points could not be evenly divided by the specified number of intervals, we calculated the maximum number of full data points that could fit into each interval using integer division. We then determined the total number of data points that this would cover and truncated the data set to include only this divisible portion. This ensures that each 20-s interval contains the same number of data points. This was to be done for the particle, magnetic field, and time series data. The field data are transformed into a matrix in Field-Aligned Coordinates (FAC) to align fluctuations with the mean magnetic field. The transformation is as follows: The mean-field aligned coordinate system (MFAC) is defined such that Z is aligned with the mean magnetic field ( $B_0$ ) direction, so that  $X_{MFAC} = X_{GSE} \times B_0$ ,  $Y_{MFAC} = B_0 \times (B_0 \times X_{GSE})$ , and  $Z_{MFAC} = B_0$  (Belcher & Davis, 1971; Matthaeus et al., 1990). We hereafter drop the “MFAC” subscript.

Simultaneously, the average solar wind speed for the subinterval was calculated and stored. Since we selected time intervals where MMS-1 was in the pristine solar wind without transients in speed, we felt that taking an average solar wind speed was appropriate. Utilizing the average speed, we calculate the distance the solar wind traveled within the time interval.

### 2.4. Correlation Analysis

Correlation functions have been widely used in the field of solar wind turbulence to investigate statistical properties of turbulent fluctuations of key parameters such as velocity, density, and magnetic field strength (Matthaeus et al., 1990). Two common tools for such analysis are the autocorrelation functions (ACF) and second-order structure functions (SF), which offer complementary insights. The ACF measures how correlated a signal is with itself at different lags, making it a direct probe of spatial or temporal coherence. However, it can be sensitive to noise, especially at longer lags. In contrast, the SF quantifies the mean squared difference between values at different lags, making it more robust to noise and better suited to capturing small-scale variability. Because SF is often more convergent and less susceptible to statistical fluctuations, particularly in turbulent and noisy intervals, deriving the ACF from the SF can yield a more stable and physically interpretable correlation profile. This redundancy also serves as a valuable cross-check for consistency between methods.

In this analysis we employ both ACF and SF techniques to mean magnetic field data in MFAC. We use solar wind speeds to convert temporal lags into spatial scales under the Taylor hypothesis for the correlation analysis (Dasso et al., 2005; Taylor, 1938).



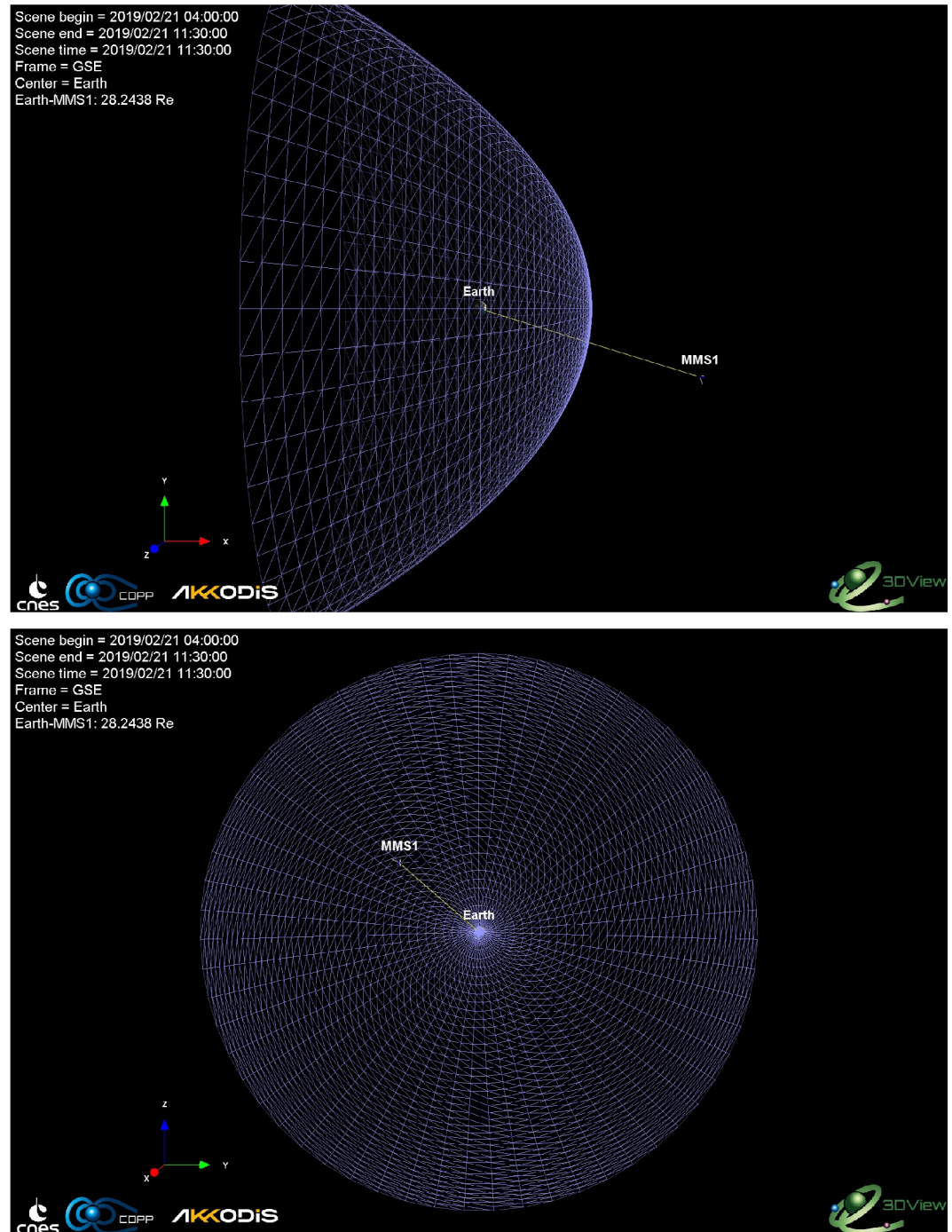


**Figure 2.** MMS-1's location relative to Earth and the Fairfield bow shock. The top panel is a top down in the XY GSE plane. The bottom panel is a head-on view in the ZY GSE plane for the same time period. MMS-1 was on the dawn side, approximately  $28.2 R_E$  from Earth.

We compute the ACF and SF for each magnetic field component in MFAC. The normalized forms (Equations 2 and 4) remove amplitude dependence, enabling comparison across intervals. The un-normalized ACF for the X component is calculated by:

$$A_L = \frac{1}{N} \sum_{n=1}^{N-L} X_n \cdot X_{n+L}. \quad (1)$$

where  $A_L$  is the ACF at lag  $L$ ,  $N$  represents the total number of data points,  $X_n$  is the mean-subtracted value of the  $X$  component at position  $n$ , and  $X_{n+L}$  is the value at the lagged position  $n + L$ . The ACF constitutes the product of  $X_n$  and  $X_{n+L}$  summed for  $N - L$  points.

The normalized ACF is given by:

$$A_{\text{norm},L} = \frac{N}{N-L} \frac{\sum_{n=1}^{N-L} X_n \cdot X_{n+L}}{\sum_{n=1}^N X_n^2}. \quad (2)$$

The denominator is the autocorrelation at zero lag, otherwise known as the variance. Employing the normalized ACF removes the fluctuation level from the subsequent averages which can be desirable.

Similarly, the un-normalized SF is computed using Equation 3, where  $S^{(2)}$  is the second order structure function,  $X(x)$  is the MFAC data,  $X(x + L)$  is the lagged data and  $\langle \rangle$  denotes the expectation value

$$S^{(2)}(L) = \langle (X(x+L) - X(x))^2 \rangle. \quad (3)$$

Likewise, the normalized SF is calculated by:

$$S_{\text{norm}}^{(2)} = \frac{\langle (X(x+L) - X(x))^2 \rangle}{\langle X(x)^2 \rangle}. \quad (4)$$

The normalized SF and the normalized ACF are related and can be derived starting with Equation 4. We begin with expanding the numerator using the identity  $(a - b)^2 = a^2 + b^2 - 2ab$ :

$$S_{\text{norm}}^{(2)}(L) = \frac{\langle X(x+L)^2 \rangle + \langle X(x)^2 \rangle - 2\langle X(x+L)X(x) \rangle}{\langle X(x)^2 \rangle}. \quad (5)$$

Assuming the signal is stationary, we have  $\langle X(x)^2 \rangle = \langle X(x+L)^2 \rangle = \langle X^2 \rangle$ , and the cross term  $\langle X(x+L)X(x) \rangle$  becomes the autocovariance at lag  $L$ . Substituting gives:

$$S_{\text{norm}}^{(2)}(L) = \frac{2\langle X^2 \rangle - 2\langle X(x+L)X(x) \rangle}{\langle X^2 \rangle}. \quad (6)$$

We then simplify to obtain:

$$S_{\text{norm}}^{(2)}(L) = 2 - 2 \cdot \frac{\langle X(x+L)X(x) \rangle}{\langle X^2 \rangle}, \quad (7)$$

and then substitute Equation 2 into Equation 7 to express the normalized SF in terms of the normalized ACF:

$$S_{\text{norm}}^{(2)}(L) = 2(1 - A_{\text{norm},L}), \quad (8)$$

which can be rearranged to express the normalized ACF as:

$$A_{\text{norm},L} = 1 - \frac{S_{\text{norm}}^{(2)}(L)}{2}. \quad (9)$$

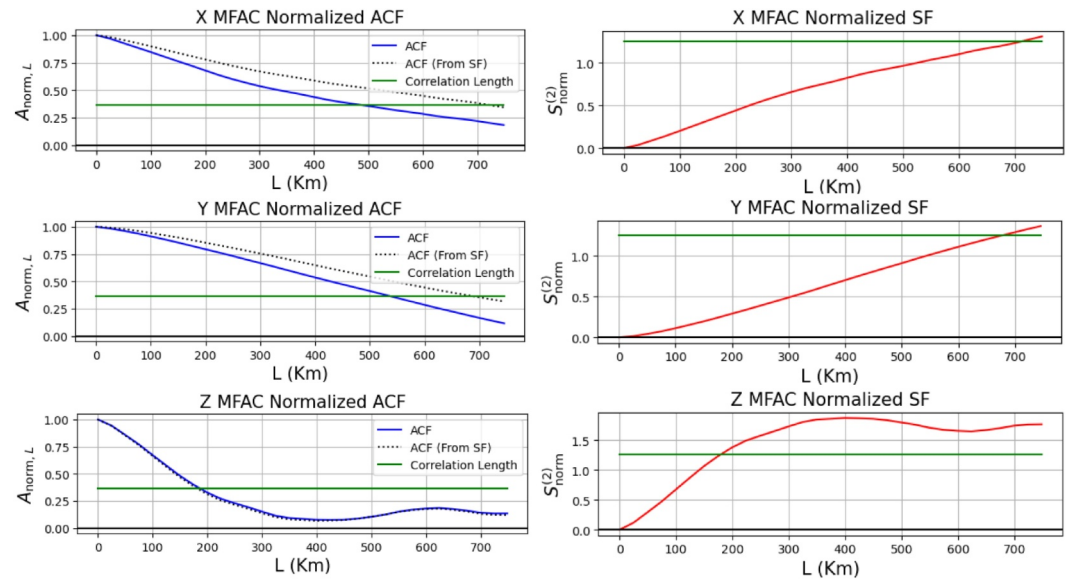


**Figure 3.** Normalized autocorrelation (blue) and structure functions (red) for X, Y, and Z MFAC components over a 20-s interval on 21 February 2019, 04:02:20 UTC. The green line marks the  $1/e$  correlation value and its intersection with the ACF denotes the normalized correlation length. This holds for the corresponding correlation length for the SF. The compressional component (Z) has the shortest correlation length, followed by transverse components (X, Y), indicating more dynamic turbulence in the compressional direction. The dotted line represents the ACF reconstructed from the SF. In this specific 20-s interval, the reconstructed ACF exhibits a longer correlation length for X and Y when compared to the directly computed ACF.

Utilizing Equations 1–4, we calculate the ACF and SF's for each 20-s interval of time for each MFAC component allowing us to compare correlation lengths across the entire time period. Equations 8 and 9 provide a consistency check by allowing the ACF to be derived from the SF, and by improving reliability in noisy intervals. In all the above formulas, Y and Z components can replace X to calculate their corresponding ACF and SF values.

### 3. Analysis and Results

#### 3.1. Autocorrelation and Second-Order Structure Function Analysis

Figure 3 shows an example of a calculated normalized autocorrelation and structure function in mean field coordinates over a 20-s interval. The green line represents the standard correlation length of  $1/e$ ; where the normalized ACF decays from 1 at zero lag to  $1/e$ . In the normalized SF plots, the green line marks the equivalent correlation length, which corresponds to a value of approximately 1.26 (see Equation 8 and replace  $A_{\text{norm},L}$  with  $1/e$ ). The point where either the ACF or SF intersects the green line is the correlation length for a given component's 20 s interval. In the top panel are the X components, followed by Y and Z in the middle and bottom panels, respectively.

We chose to adopt the 10% cosine taper (Matthaeus & Goldstein, 1982) where the maximum spatial lag is determined to be 10% of the total length of our data. Given that we are looking at sub-intervals of 20-s data, our resultant maximum lag is 2 s. The data show that, in this interval, Z, the compressional component, has the shortest correlation length, followed by X and Y. These finite correlation lengths on the order of 100's of kilometers show that the correlation analysis is capable of observing small scale turbulence within the ion dissipation range.

The normalized second order structure functions, nearly inversely mirror the behavior of the autocorrelation functions during this interval. The Z, compressional component, has the shortest correlation length, followed by the transverse components Y and X.

The normalized ACF reconstructed from the SF reflects the behavior of the SF; although the Z component has the shortest correlation length, the Y component has a shorter correlation length (~684 km) than the X component (~718 km)—opposite with what is observed in the directly computed ACF. While the X and Y components



deviate more from the nominal ACF than the  $Z$  component in this case, this behavior is not consistent across other 20-s intervals. No single component of the reconstructed ACF consistently matches the directly computed ACF across all time intervals.

Due to the normalized nature and the short time interval shown in Figure 3, we were able to reduce much of the turbulent power level that would typically dominate the computed correlation function at larger scales and convert it into the contributions to the local mean magnetic field. This enables us to use the cone angle for the 20-s interval to explore the underlying geometry of the turbulent dissipation range.

In total, we performed an ACF and SF analysis on 1,350 non-overlapping, 20-s intervals. For each interval, the resulting ACF and SF were summed and averaged across all intervals. Figure 4 shows the normalized average autocorrelation function—our primary analysis method—alongside the normalized second-order structure function and the SF-reconstructed ACF.

When looking at the average of the normalized ACF in Figure 4 we see correlation lengths in the  $X$ ,  $Y$  and  $Z$  components around  $\sim 750$ ,  $\sim 690$  and  $\sim 550$  km respectively. These correlation lengths are on the order of what is considered to be the ion dissipation range. We observe that the compressional component of the magnetic field exhibits the shortest spatial correlation length, followed by the two transverse components. This suggests the presence of enhanced dissipation processes in the compressional component, contributing to field aligned anisotropy relative to the perpendicular components. Among the transverse components, the  $X$  component exhibits a shorter correlation length than  $Y$  component over this 20-s interval, indicating anisotropy within the perpendicular plane to the mean magnetic field.

The average normalized SF displays a similar, though inverted, behavior to the normalized ACF across all three components, with slightly longer correlation lengths. As a result, the reconstructed ACF also displays longer correlation lengths when compared to the directly computed normalized ACF for each component.

Next, we examine the dependence of ACF correlation lengths on the cone angle  $\Theta_{BV}$ . The cone angle ( $\theta_{BV}$ ) is defined as the angle between the IMF (along ZMFAC) and the solar wind direction, such that  $0^\circ \leq \Theta_{BV} \leq 90^\circ$ . We calculated the average  $\Theta_{BV}$  in each of the 1,350, 20-second intervals. The distribution of the resultant  $\Theta_{BV}$  values can be seen in Figure 5.

In Figure 5, we can see that a majority of the intervals have an average  $\Theta_{BV}$  closer to  $90^\circ$  that exceeds the average Parker Spiral angle measured in observations at 1 AU,  $\Theta_{BV} > 45^\circ$  (Svalgaard & Wilcox, 1974). While the overall high  $\Theta_{BV}$  distribution in Figure 5 suggests that the ion foreshock likely has a limited contribution to our observations, magnetic connectivity to the bow shock is still expected given MMS-1's location near the shock. The close proximity allows for reflected particles to reach the spacecraft. This effect may be even more pronounced for the electron foreshock region which extends even further into space. That said, we expect that this contribution will remain relatively low at high angles ( $\Theta_{BV} \geq 45^\circ$ ).

### 3.2. Cone Angle Dependence

By utilizing high resolution data and short time intervals, we have demonstrated that correlation function analysis yields finite correlation lengths, which are on the order expected of the ion-dissipation range. We wanted to further explore how the cone angle shown in Figure 5 affected the observations during this interval. To this end, we paired each ACF interval with its respective average  $\Theta_{BV}$  and dropped it into bins ranging from  $0^\circ$  to  $90^\circ$  with  $10^\circ$  increments. Once all respective intervals were placed into the appropriate bins, we then took the average of each ACF within each bin and calculated the respective SEM for each lag value. Figure 6 depicts the average correlated normalized ACF for all three components associated with its respective  $\Theta_{BV}$ .

The red line represents the standard normalized correlation length of  $1/e$  that had been used in the prior normalized ACF analysis above. The  $X$  component is represented by the blue line,  $Y$  is represented by the orange line, and  $Z$  is represented by the green line. The legend displays the total number of samples within each angular range, as well as the correlation lengths for cases where correlation is achieved within this spatial lag range. The approximate correlation lengths were estimated by interpolating the points where the correlation function crossed the  $1/e$  threshold.

By separating the correlation functions into their respective angular bins and comparing the overall correlation lengths we find that the correlation lengths associated with the compressional component continue to be shorter

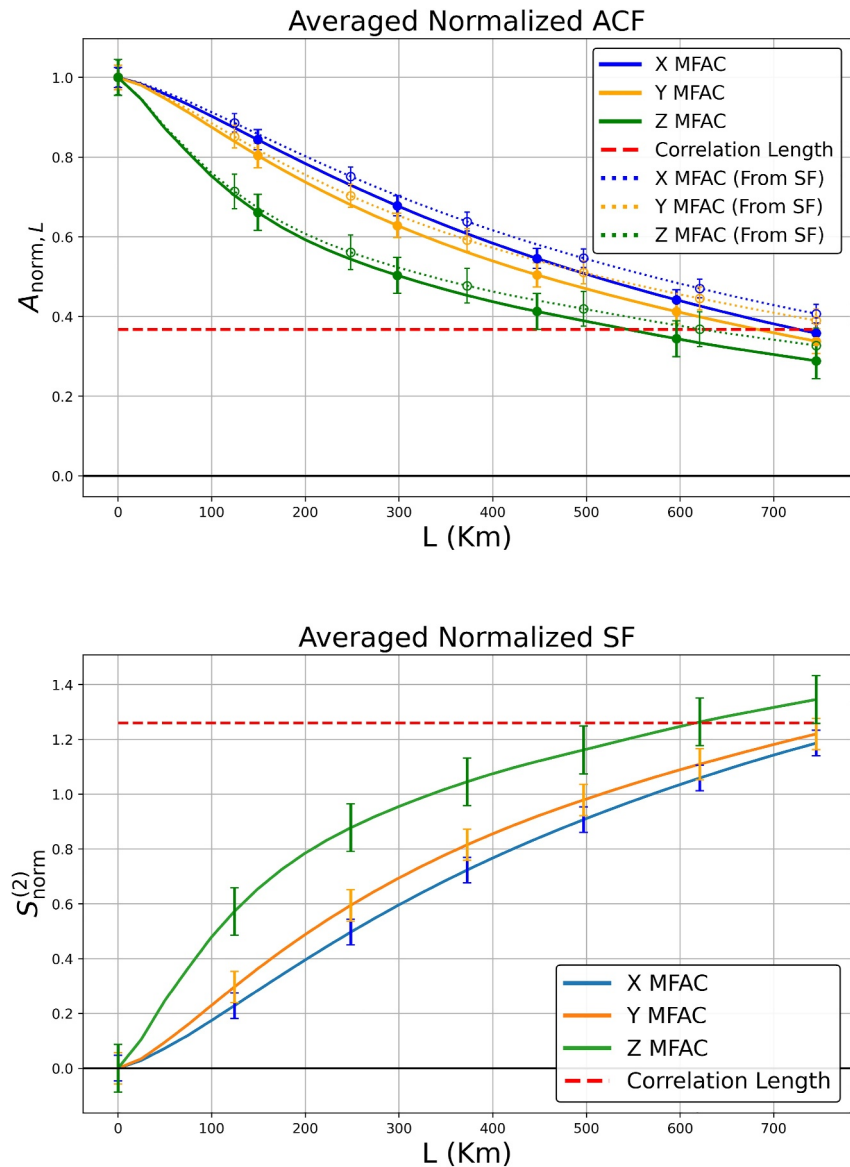


**Figure 4.** Average normalized autocorrelation (top) and structure functions (bottom) for X (blue), Y (orange), and Z (green) MFAC over 7.5 hr. The respective dotted lines in the top plot represent the ACF reconstructed from the SF for X (blue dots), Y (orange dots), and Z (green dots). The error bars represent the standard error of the mean (SEM), with closed dots representing the normalized ACF SEM and the open dots representing the ACF reconstructed from the SF SEM. The red dashed line marks the respective ACF and SF correlation length. The compressional component (Z) has a correlation length at  $\sim 550$  km, while transverse components (X, Y) have correlation lengths at  $\sim 750$  km and  $\sim 700$ , indicating more dynamic dissipative processes in the compressional direction at dissipation scales and anisotropy in the transverse components. The reconstructed ACF displays longer correlation lengths overall when compared to the directly computed ACF.

than those in the transverse components across most cone angles. In addition, with the exception of the correlation functions at the smallest angles (Figures 6a–6c), we observe the correlation lengths of the X component exceeding those of the Y component. The X and Y correlation functions also exhibit a non-monotonic increase in their separation as  $\theta_{BV}$  increases from  $30^\circ$  to  $90^\circ$ .

It is important to note that due to the limited number of small angles in this selected time window, the correlation functions at smaller angular bins exhibit larger standard errors of the mean. Specifically, Figures 6a–6c contain an order of magnitude fewer samples than the subsequent plots. Figure 6c in particular, appears anomalous, as the Z component appears to have a longer correlation length than both transverse components—contrary to the trend

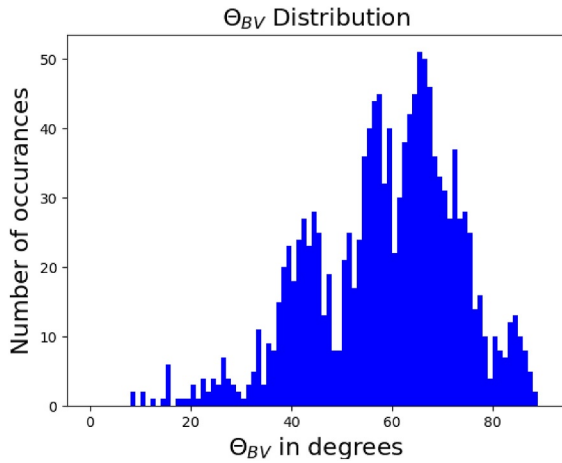


**Figure 5.** This figure shows the average  $\Theta_{BV}$  of each 20-s interval in the total 7.5 hr timeframe. We see that there is a skew toward higher  $\Theta_{BV}$  bins in this particular data set. Due to the location of MMS, ion foreshock interactions limit the amount of data collected from small angle bins.

observed across the broader data set. We address these discrepancies in detail later in the paper and provide supporting evidence for our interpretation.

Figure 7 depicts the reconstructed normalized ACF grouped by cone angle bins in a similar manner to Figure 6. As seen with the previous figure, the SF-reconstructed ACF exhibit longer correlation lengths compared to those directly computed from the ACF. The trend observed in Figure 6 also persists; in the high angle bins ( $30^{\circ}$ – $90^{\circ}$ ), the compressional component (Z) displays the shortest correlation lengths relative to the transverse components (X and Y). Furthermore, the transverse components are not isotropic—Y consistently exhibits shorter correlation lengths than X across the high-angle bins.

Alongside the analysis performed in Figures 6 and 7, we computed ideal exponential fits for each angle averaged ACF and SF-reconstructed ACF to compare the corresponding idealized correlation lengths with the ones derived from the data. Table 2 summarizes the results corresponding to Figures 6 and 7 and their associated fits. The first column lists the angular range and the second column identifies the component analyzed. The third column presents the 1/e correlation length (crossing point) derived from the ACF for both the data and model fit, along with their associated uncertainties. The fourth column provides the same information for the SF reconstructed ACF shown in Figure 7.

Uncertainties for the data-based crossings were calculated using linear interpolation between the two points on either side of 1/e, and then the errors were propagated utilizing the SEM, while uncertainties for the model-based crossings represent the standard deviation derived from the covariance matrix of the fit. Asterisks (\*) denote values obtained through extrapolation.

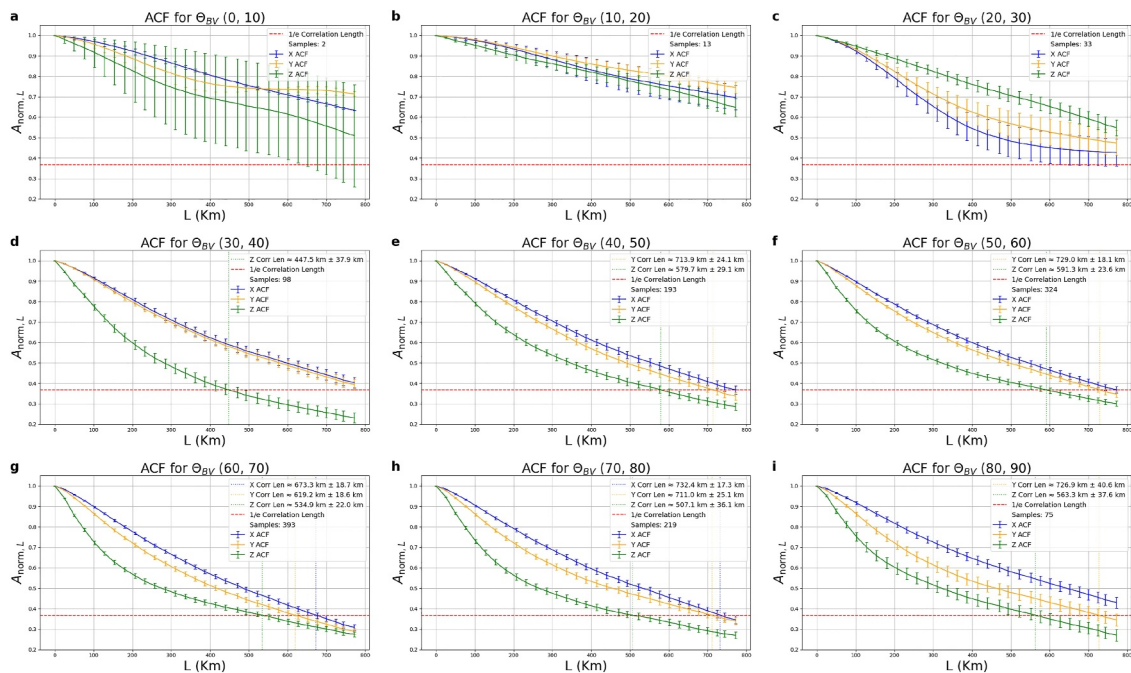


**Figure 6.** Averaged normalized autocorrelation functions grouped by average ( $\Theta_{BV}$ ) in ascending order: (a)  $0^{\circ}$ – $10^{\circ}$ , (b)  $10^{\circ}$ – $20^{\circ}$ , (c)  $20^{\circ}$ – $30^{\circ}$ , (d)  $30^{\circ}$ – $40^{\circ}$ , (e)  $40^{\circ}$ – $50^{\circ}$ , (f)  $50^{\circ}$ – $60^{\circ}$ , (g)  $60^{\circ}$ – $70^{\circ}$ , (h)  $70^{\circ}$ – $80^{\circ}$ , (i)  $80^{\circ}$ – $90^{\circ}$ . Blue, orange, and green lines represent X, Y, and Z MFAC components, respectively; the dashed red line marks the 1/e correlation length. Error bars show the standard error of the mean. The legend also indicates the number of samples in each angular range, along with the correlation lengths where they are defined in this lag range. The compressional component (Z) consistently exhibits shorter correlation lengths than transverse components (X, Y) across most angular ranges, indicating more dynamic fluctuations in the compressional direction. The departure between X and Y appears to increase with increasing  $\theta_{BV}$  between  $30^{\circ}$  and  $90^{\circ}$ .

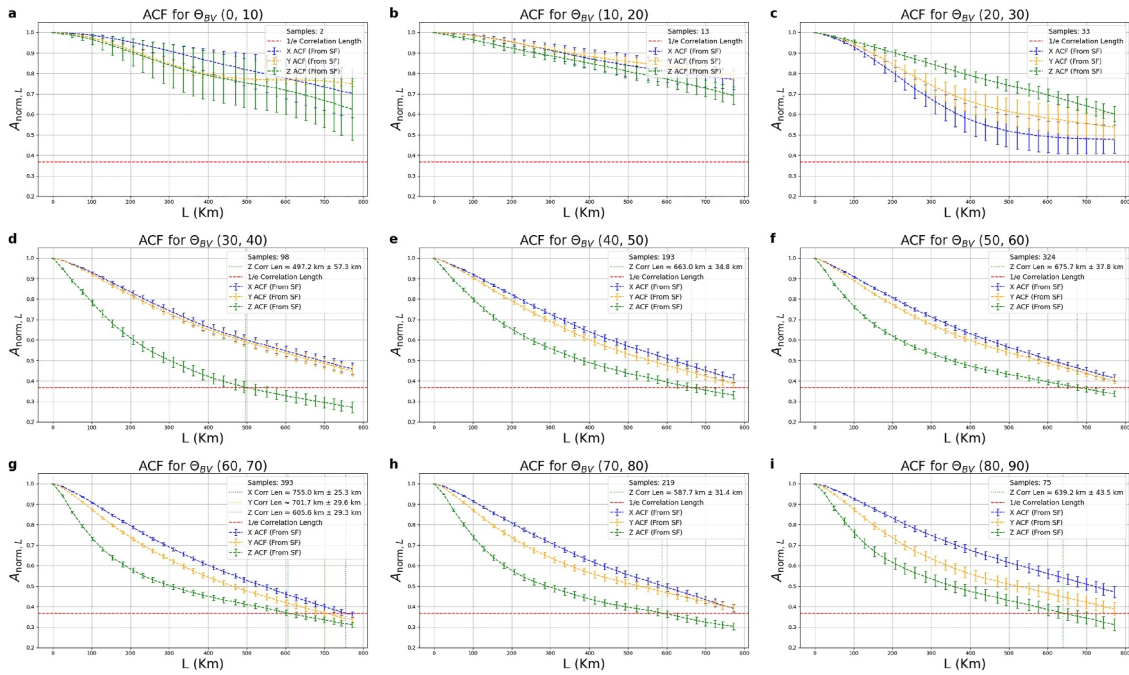


**Figure 7.** Normalized SF reconstructed ACF grouped by  $\Theta_{BV}$  bins for X (blue), Y (orange), and Z (green) MFAC components in ascending order: (a)  $0^{\circ}$ – $10^{\circ}$ , (b)  $10^{\circ}$ – $20^{\circ}$ , (c)  $20^{\circ}$ – $30^{\circ}$ , (d)  $30^{\circ}$ – $40^{\circ}$ , (e)  $40^{\circ}$ – $50^{\circ}$ , (f)  $50^{\circ}$ – $60^{\circ}$ , (g)  $60^{\circ}$ – $70^{\circ}$ , (h)  $70^{\circ}$ – $80^{\circ}$ , (i)  $80^{\circ}$ – $90^{\circ}$ . The red dashed line marks the  $1/e$  correlation length. Error bars represent the standard error of the mean. The legend also indicates the number of samples in each angular range, along with the correlation lengths where they are defined in this lag range. The compressional component (Z) continues to display shorter correlation lengths than the transverse components (X, Y) across most angular ranges. Compared to the directly computed ACFs shown in Figure 6, the correlation lengths derived by the reconstructed ACF are generally longer.

The first three rows are highlighted in gray to indicate reduced reliability due to the limited data within those small-angle bins; these values should be interpreted with caution. Looking to the higher-angle bins ( $30^{\circ}$ – $90^{\circ}$ ), a consistent trend is observed: The Z component (compressional) exhibits the shortest correlation length in both the raw data and fits model, followed by the Y component, and then the X component. The largest difference between X and Y correlation lengths is found in the  $80^{\circ}$  to  $90^{\circ}$  bin when MMS-1 samples fluctuations nearly perpendicular to  $\mathbf{B}_0$ . This ordering also holds in the correlation lengths associated with the SF-reconstructed ACF. Across all components, the reconstructed ACF consistently shows longer correlation lengths than those obtained from the direct ACF calculations. The results from Table 2 can be visualized in Figure 8.

Figure 8 presents the correlation lengths derived from both the directly computed ACF and the SF-reconstructed ACF, plotted as a function of  $\Theta_{BV}$ . In this visualization of the correlation lengths from Figures 6 and 7 along with Table 2, the results are separated by component: X (blue), Y (orange), and Z (green). The plots differentiate between values obtained directly from the data and those obtained from model fits, as well as the two ACF analysis—the raw ACF from Figure 6 and the SF-reconstructed ACF from Figure 7.

To aid visual interpretation, different marker styles are used. ACF data points are denoted by  $X'$ s, ACF fits by circles; SF-reconstructed ACF data by stars, and their corresponding fits by squares. A solid black line is included to represent the expected behavior of pure 2D turbulence, where the correlation length varies as  $\sin^{-1} \theta_{BV}$ , while a dotted black line represents the expected behavior of pure slab turbulence, with the correlation length varying as  $\cos^{-1} \theta_{BV}$ . The two curves are placed to intersect each other at a lag value of 650 km in the  $60^{\circ}$  to  $70^{\circ}$  bin where the data most closely resembles the behavior of the inverse sine (pure 2D turbulence) and inverse cosine (pure 1D turbulence) reference lines. Data for X and Y in Figure 8 at large angles ( $30^{\circ}$ – $90^{\circ}$ ) exhibits a similar, but weaker dependence on  $\theta_{BV}$  compared to the  $\sin^{-1} \theta_{BV}$  scaling expected for pure 2D turbulence. Data for Z is less clear with regard to its dependence on  $\sin^{-1} \theta_{BV}$  in this same range. At the same time, there is little to no dependence on  $\theta_{BV}$  compared to the  $\cos^{-1} \theta_{BV}$  scaling expected for pure slab turbulence. This suggests that 2D turbulence is dominant, while there also exists a small contribution from slab-like turbulence. To quantify our results, we created a mixed best fit model — denoted by the black dotted line, that combines the inverse sine and

**Table 2**  
Summary of ACF and Reconstructed SF-ACF Correlation Lengths

$\Theta_{BV}$	Component	ACF CL [Data — Fit](km)	SF-ACF CL [Data — Fit](km)
(0, 10)	X	$1,242^* \pm 2 \times 10^1$	$1,589^* \pm 2 \times 10^1$
	Y	$1,828^* \pm 6 \times 10^1$	$2,227^* \pm 7 \times 10^1$
	Z	$1,122^* \pm 1 \times 10^1$	$1,300^* \pm 2 \times 10^1$
(10, 20)	X	$1,448^* \pm 2 \times 10^1$	$1,966^* \pm 3 \times 10^1$
	Y	$1,769^* \pm 2 \times 10^1$	$2,221^* \pm 3 \times 10^1$
	Z	$1,357^* \pm 6$	$1,622^* \pm 1 \times 10^1$
(20, 30)	X	$732^* \pm 2 \times 10^1$	$848^* \pm 2 \times 10^1$
	Y	$904^* \pm 1 \times 10^1$	$1,105^* \pm 2 \times 10^1$
	Z	$1,034^* \pm 5$	$1,221^* \pm 6$
(30, 40)	X	$848^* \pm 7$	$998^* \pm 8$
	Y	$820^* \pm 6$	$960^* \pm 6$
	Z	$447 \pm 4 \times 10^1$ — $444 \pm 8$	$497 \pm 6 \times 10^1$ — $491 \pm 1 \times 10^1$
(40, 50)	X	$801^* \pm 9$	$900^* \pm 8$
	Y	$706 \pm 2 \times 10^1$ — $714 \pm 6$	$809^* \pm 5$
	Z	$579 \pm 3 \times 10^1$ — $532 \pm 1 \times 10^1$	$662 \pm 3 \times 10^1$ — $592 \pm 1 \times 10^1$
(50, 60)	X	$777^* \pm 5$	$882^* \pm 4$
	Y	$729 \pm 2 \times 10^1$ — $708 \pm 3$	$814^* \pm 6$
	Z	$591 \pm 2 \times 10^1$ — $520 \pm 2 \times 10^1$	$676 \pm 4 \times 10^1$ — $571 \pm 2 \times 10^1$
(60, 70)	X	$673 \pm 2 \times 10^1$ — $693 \pm 8$	$755 \pm 3 \times 10^1$ — $785 \pm 7$
	Y	$619 \pm 2 \times 10^1$ — $605 \pm 3$	$702 \pm 3 \times 10^1$ — $680 \pm 4$
	Z	$534 \pm 2 \times 10^1$ — $475 \pm 2 \times 10^1$	$606 \pm 3 \times 10^1$ — $524 \pm 2 \times 10^1$
(70, 80)	X	$732 \pm 2 \times 10^1$ — $764 \pm 8$	$856^* \pm 7$
	Y	$710 \pm 3 \times 10^1$ — $665 \pm 7$	$752^* \pm 1 \times 10^1$
	Z	$507 \pm 4 \times 10^1$ — $468 \pm 2 \times 10^1$	$588 \pm 3 \times 10^1$ — $510 \pm 2 \times 10^1$
(80, 90)	X	$929^* \pm 6$	$1,038^* \pm 6$
	Y	$727 \pm 4 \times 10^1$ — $678 \pm 8$	$745^* \pm 1 \times 10^1$
	Z	$563 \pm 4 \times 10^1$ — $511 \pm 1 \times 10^1$	$639 \pm 4 \times 10^1$ — $560 \pm 2 \times 10^1$

cosine dependencies. Using a non-linear regression model, we determined the relative contributions of each of the components to the line of best fit. We determined that the fit with the highest  $R^2$  value ( $R^2 = 0.645$ ) consisted of 95.4% inverse sine and 4.6% inverse cosine contributions.

To understand the discrepancies observed in small angles in Figures 6 and 7 and Table 2, we created a series of plots showing the correlation value as a function of time. We selected a spatial lag value of 400 km to base these graphs on since it represented the midpoint in most of the previous correlation plots. These plots helped to identify potential patterns in the data that may indicate the presence of back-streaming particles and their associated wave activity that are likely resulting from being magnetically well connected to the shock at small cone angles.

Figure 9 presents these correlation value versus time plots across the X, Y, and Z axes. The dots in the plot are color-coded to represent specific angular ranges. Cyan dots represent the angular range from  $0^\circ \leq \Theta_{BV} \leq 10^\circ$ , red dots  $10^\circ \leq \Theta_{BV} \leq 20^\circ$ , green dots  $20^\circ \leq \Theta_{BV} \leq 30^\circ$ , orange dots  $30^\circ \leq \Theta_{BV} \leq 40^\circ$ , purple dots  $40^\circ \leq \Theta_{BV} \leq 50^\circ$ , blue dots  $50^\circ \leq \Theta_{BV} \leq 60^\circ$ , brown dots  $60^\circ \leq \Theta_{BV} \leq 70^\circ$ , magenta dots  $70^\circ \leq \Theta_{BV} \leq 80^\circ$  and gold dots  $80^\circ \leq \Theta_{BV} \leq 90^\circ$ . We observe two clusters of small angles, ( $0^\circ$ – $30^\circ$ ) between 09:30–10:00 and 10:30–10:50 UTC. This could suggest periods of aligned magnetic field and solar wind velocity. Additionally, there are no large-scale structures evident in Figure 9, indicating that turbulence dominates the overall dynamics.



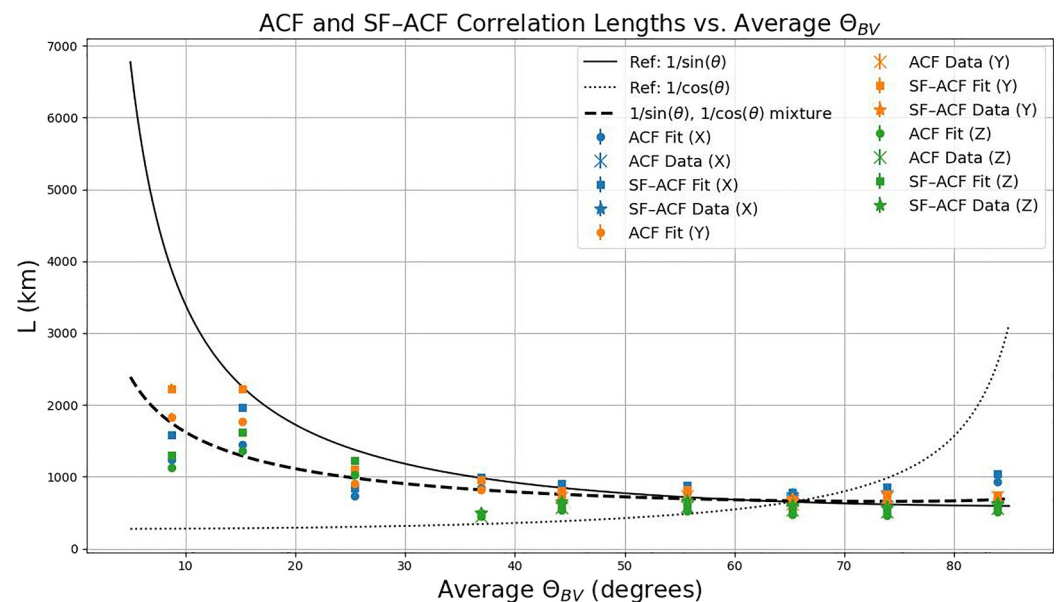


**Figure 8.** Correlation lengths derived from both the raw ACF and the SF-reconstructed ACF are plotted against the average  $\Theta_{BV}$ . The plot is divided by component: X (blue), Y (orange), and Z (green). It distinguishes between data and model fits, as well as correlation lengths obtained from the directly computed ACF (Figure 6), and the SF-reconstructed ACF (Figure 7). Symbols denote the source and method: ACF data are marked with *asterisks*, ACF fits with *circles*; SF-reconstructed ACF data are shown as *stars*, and SF-reconstructed ACF fits as *squares*. Pure 2D turbulence would have correlation lengths vary as  $\sin^{-1} \theta_{BV}$ , which is represented by the solid black line. Pure slab turbulence would have correlation lengths vary as  $\cos^{-1} \theta_{BV}$ , which is represented by the dotted black line. The curves are positioned so as to intersect each other at a lag of 650 km in the  $60^\circ$  to  $70^\circ$  bin. The correlation functions tend to follow the solid black line which suggests the dominance of 2D turbulence. This is further supported with the inclusion of a best fit line denoted by the blacked dashed line. Using a non-linear regression model, we were able to determine the approximate contributions from the inverse sine and cosine functions to the curve fit. We found that the best fit line was comprised of 95.4% inverse sine and 4.6% inverse cosine contributions.

### 3.3. Energetic Particle Analysis

Although no clear pattern emerges in the distribution of correlation values across angles over time, there is a distinct clustering of small angle data points between 09:45 and 10:00 UTC and then again between 10:30 and 10:50 UTC. These periods coincide with energy spikes in the EIS, Energy-by-Time of Flight (ExTOF) proton energy spectra, seen in Figure 10. The study did not utilize the Pulse Height-by-Time of Flight (PHxTOF) flux due to sunlight-induced contamination resulting from the spacecraft's tilt during the 2019 solar wind turbulence campaign.

The top plot in Figure 10 depicts the ExTOF proton energy from 50 to 200 keV with its associated flux in units of  $\text{cm}^{-2} \text{sr}^{-1} \text{s}^{-1} \text{keV}^{-1}$ . The bottom plot is the ExTOF proton pitch angle distribution (PAD) in the 50 keV channel with angle in units of degrees on the Y-axis and proton flux in units of  $\text{cm}^{-2} \text{sr}^{-1} \text{s}^{-1} \text{keV}^{-1}$ . The clustering of small cone angles seen in Figure 9, coupled with the spikes in proton energy over the same time periods and the large variations in proton PAD (09:45–10:00 UTC and 10:30–10:50 UTC) in Figure 10 suggest a period of strong magnetic connectivity to the bow shock. This likely facilitates the presence of back-streaming particles and their associated wave activity which we observe in Figure 11.

In Figure 11, the magnetic time series for these two intervals reveals additional signatures supporting this interpretation. The top panel (09:45–10:00 UTC) exhibits clear sinusoidal oscillations, indicative of wave activity, while possible magnetic field discontinuities are present in the bottom panel (10:30–10:50 UTC). The presence of energetic particles, along with magnetic field oscillations suggest that energetic particles may originate from foreshock transients that modify the turbulent cascade (Weygand et al., 2009), such as hot flow anomalies (Paschmann et al., 1988; Schwartz, 1995; Thomas et al., 1991) and are not intrinsic to the solar wind dynamics.

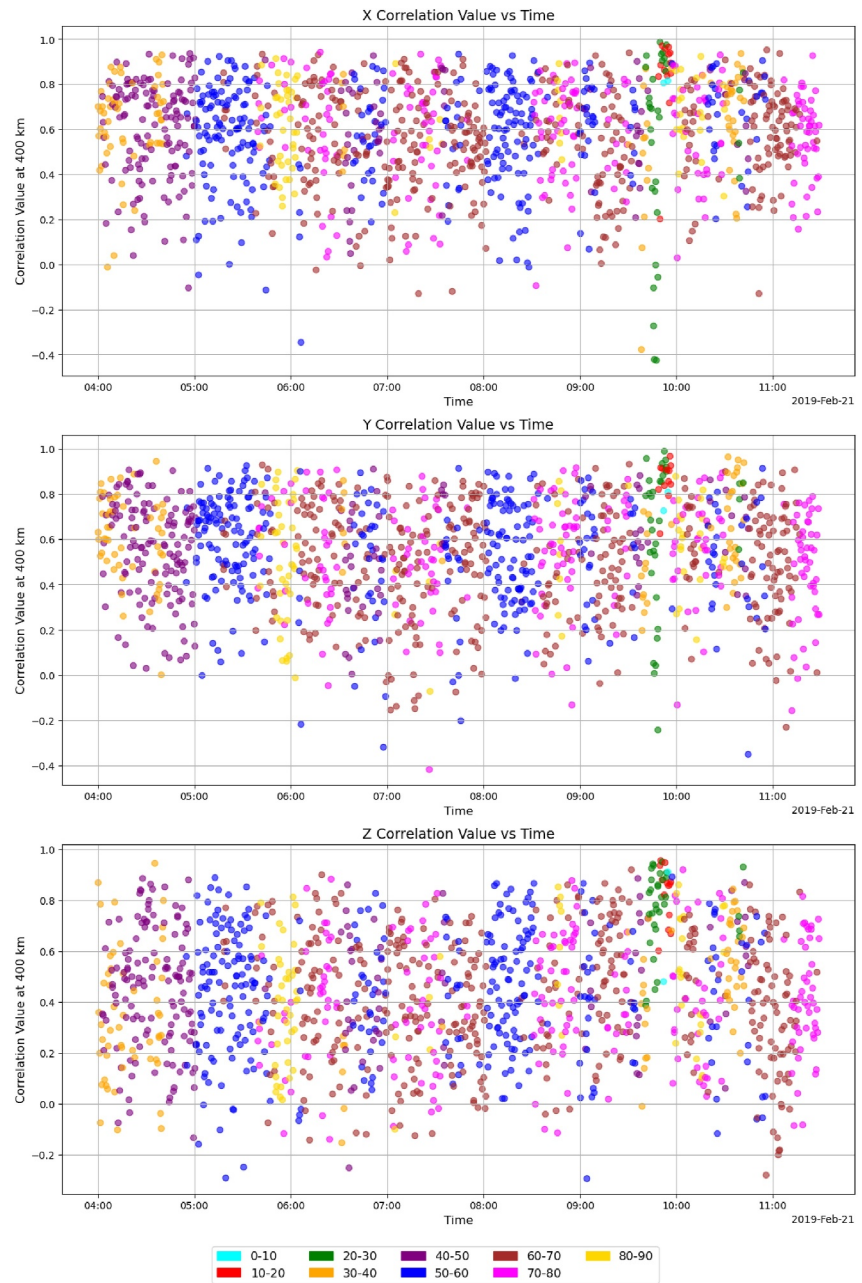


**Figure 9.** Correlation values of the normalized autocorrelation function at a 400 km spatial lag for X, Y, and Z MFAC components, colored by cone angle ranges (cyan:  $0^\circ \leq \Theta_{BV} \leq 10^\circ$ , red:  $10^\circ \leq \Theta_{BV} \leq 20^\circ$ , green:  $20^\circ \leq \Theta_{BV} \leq 30^\circ$ , orange:  $30^\circ \leq \Theta_{BV} \leq 40^\circ$ , purple:  $40^\circ \leq \Theta_{BV} \leq 50^\circ$ , blue:  $50^\circ \leq \Theta_{BV} \leq 60^\circ$ , brown:  $60^\circ \leq \Theta_{BV} \leq 70^\circ$ , magenta:  $70^\circ \leq \Theta_{BV} \leq 80^\circ$ , gold:  $80^\circ \leq \Theta_{BV} \leq 90^\circ$ ). Clustering of small angles ( $0^\circ$ – $30^\circ$ ) occurs between 09:30–10:00 and 10:30–10:50 UTC, suggesting periods of aligned magnetic field and solar wind velocity. No large-scale structures are evident, indicating turbulence dominates the dynamics.

Outside of these intervals, no significant anomalies are observed. This supports the conclusion that the majority of observed fluctuations can be attributed to small-scale turbulence as opposed to large-scale phase-coherent structures driven by outside processes such as bow-shock interactions.

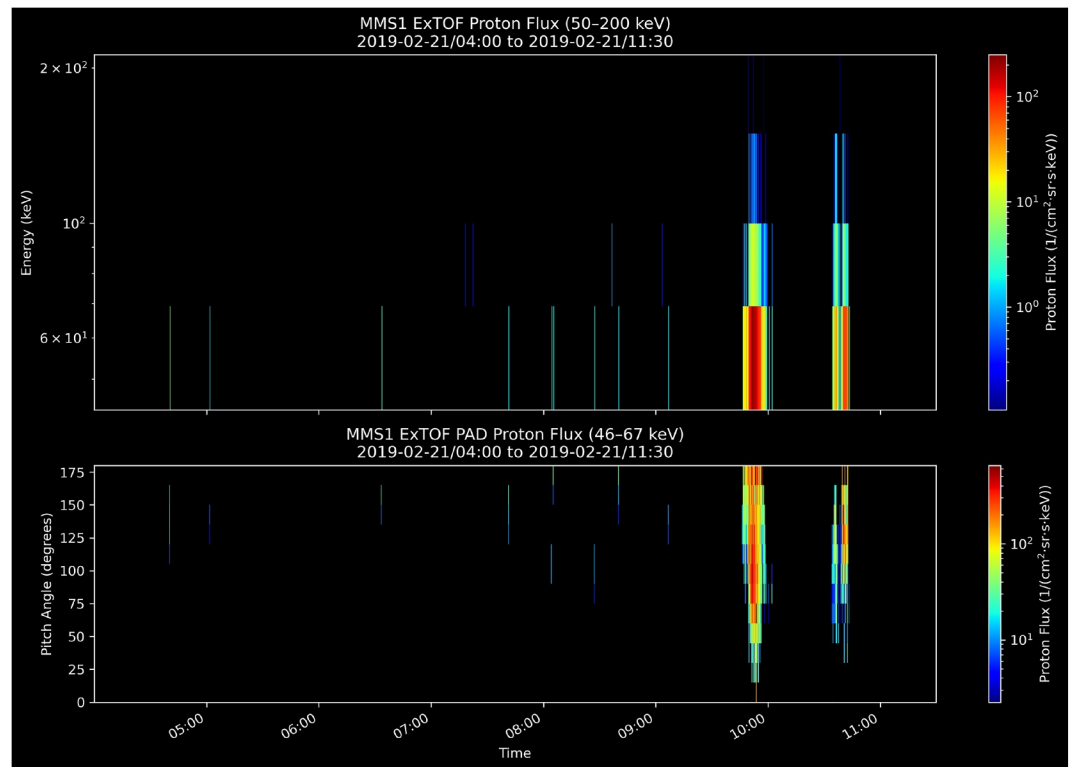


**Figure 10.** Solar wind ion energies on 21 February 2019, 04:00:00–11:30:00 UTC, from MMS-1. Top: ExTOF proton energies (keV) and flux ( $\text{cm}^{-2} \text{sr}^{-1} \text{s}^{-1} \text{keV}^{-1}$ ) Bottom: ExTOF pitch angle distributions (PAD) (degrees) and proton flux ( $\text{cm}^{-2} \text{sr}^{-1} \text{s}^{-1} \text{keV}^{-1}$ ). Ions are at background energies with the exception of intervals of time 09:45–10:00 UTC and 10:30–10:50 UTC. Energy spikes along with the PAD aligning with clustering of small angles in Figure 9 could suggest a connection to the bowshock.

#### 4. Discussion

Our findings confirm that dissipation-scale turbulence is highly anisotropic, with shorter correlation lengths in the compressional component ( $Z$ ) than transverse components ( $X$ ,  $Y$ ). This may reflect enhanced damping of compressional waves at small scales (Alexandrova et al., 2013). The dependence on cone angle suggests that turbulence is more pronounced when the magnetic field is perpendicular to the solar wind flow, consistent with quasi-2D turbulence models (Cho & Vishniac, 2000; Dasso et al., 2005; Matthaeus et al., 1996, 1998; Oughton et al., 1994; Shebalin et al., 1983; Vasquez et al., 2014).

Bieber et al. (1996) modeled turbulence as the potential combination of axisymmetric slab turbulence and axisymmetric 2D turbulence. The turbulence in the present analysis cannot be pure axisymmetric slab turbulence (a) because correlation lengths in  $X$  and  $Y$  differ and (b) there is a significant  $\delta B_z$  component. The 2D turbulence can have a  $\delta B_z$  component. Due to the divergence-free constraint, Bieber et al. (1996) showed that the spectral power in the  $X$  and  $Y$  components would differ when measured by a single spacecraft for both 2D turbulence and a mixture of slab and 2D turbulence. This difference possibly extends to correlation lengths in  $X$  and  $Y$ . A pure 2D turbulence would have the correlation lengths vary as  $\sin^{-1} \theta_{BV}$ . The actual variation in the data is weaker for correlation lengths in  $X$  and  $Y$  but relatively consistent with a predominance of energy in 2D turbulence as compared to slab turbulence. Moreover, the difference in correlation functions and lengths between  $X$  and  $Y$  appear to increase with increasing  $\theta_{BV}$  and are largest when  $\theta_{BV}$  is near  $90^\circ$ . This again indicates that 2D turbulence is more prevalent than slab turbulence.

These results advance our understanding of energy dissipation in the solar wind and have implications for heating and particle acceleration. The dissipation processes operate in the solar wind appear to damp out selectively the compressive fluctuations associated with the fluctuating parallel magnetic field because the  $Z$  component has a smaller correlation length than the  $X$  and  $Y$  components. This points to the presence of collisionless Landau and

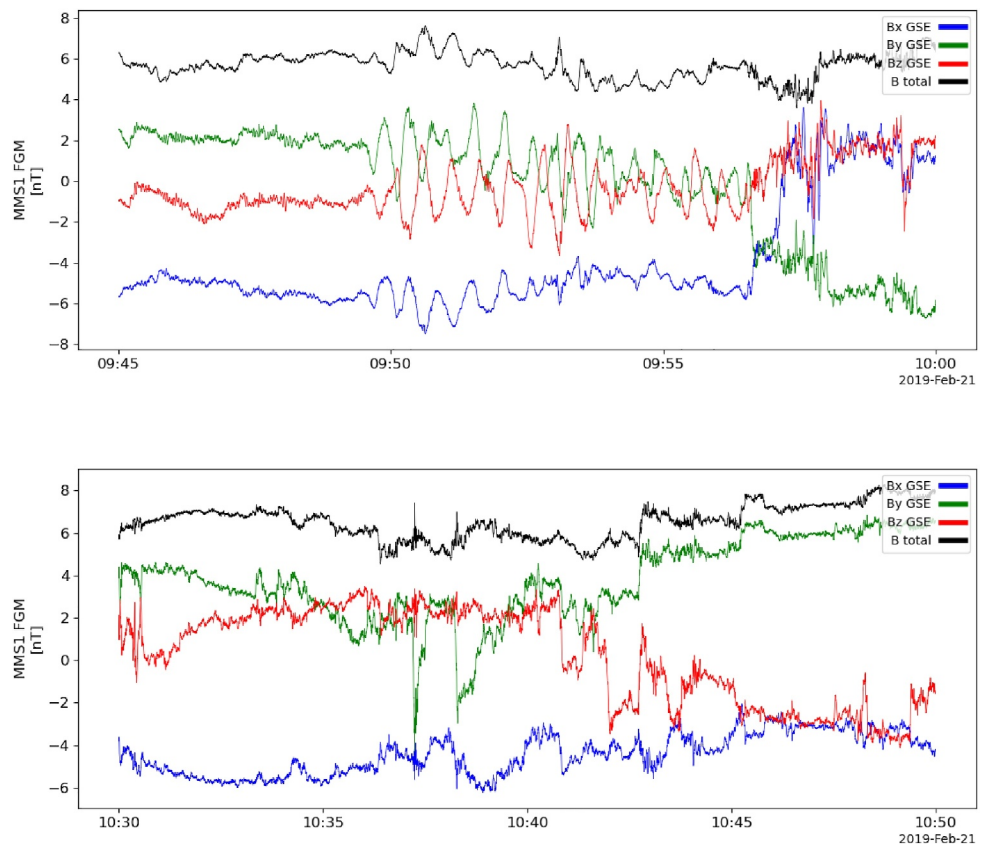


**Figure 11.** This set of time series plots for the two intervals of interest on 21 February 2019: 09:45–10:00 UTC (top plot) and 10:30–10:50 UTC (bottom plot). Sinusoidal activity is present in the top plot, indicating the presence of wave activity. The bottom plot shows signs of magnetic discontinuities, which could be associated with transient structures such as hot flow anomalies.

transient time damping (Barnes, 1966; TenBarge et al., 2013). The prevalence of 2D turbulence is consistent with a turbulent energy cascade that is most intense in the perpendicular direction with respect to  $\mathbf{B}_0$ , as numerical simulations have long indicated. Most of the energy in the 2D turbulence is associated with the X and Y components, and so even more significant kinetic processes must exist to dissipate this part of the fluctuation energy. Such processes might be associated with the demagnetization of ions on scales of the ion gyroradius (Bourouaine & Chandran, 2013; Vasquez, 2015). Effective acceleration of energetic particles comes mainly from slab turbulence-particle interactions. The reduced presence of slab like fluctuations in the solar wind has long been considered as the explanation for the long mean-free paths of energetic particles (Bieber et al., 1996).

## 5. Conclusions

Using MMS data and a modified correlation function analysis, we demonstrated that solar wind turbulence at dissipation scales has correlation lengths over short spatial scales ( $\sim 100$ – $1,000$  km), with shorter correlation lengths in the compressional component compared to the transverse components. We also observe anisotropy in the transverse components, especially at larger cone angles. These findings highlight the anisotropic nature of dissipation-scale turbulence and its dependence on solar wind conditions. Limitations include the single 7.5 hr time interval analyzed and the FGM's noise floor at high frequencies. Future work should explore additional data sets and incorporate multi-spacecraft correlations to further resolve sub-ion and electron-scale dynamics.

Using data from the MMS solar wind turbulence campaign, we used a period of time when the spacecraft was outside of Earth's bow shock, mostly free from waves and structures associated with the ion and electron fore-shock regions, where the spectral power was sufficient to surpass the FGM's inherent noise level. This allowed us to divide the larger time period into smaller segments, effectively minimizing the influence of excess power from



the lower frequency energy spectra. Subsequently, we applied correlation function analysis, supplemented by second-order structure function analysis, to investigate turbulence on scales of hundreds of kilometers, placing the observations in the ion dissipation range.

When averaged over all 20-s intervals, the parallel fluctuating magnetic field component  $Z$  had a shorter correlation length than the perpendicular fluctuating components  $X$  and  $Y$ . As the fluctuating  $Z$  component is associated with compressions, the shorter  $Z$  correlation length could indicate a greater preponderance of dissipation associated with those compressions. The correlation lengths of  $X$  and  $Y$  differed such that  $X$  was longer than  $Y$ . These trends also exist as a function of cone angle  $\theta_{BV} > 30^\circ$  where sufficient intervals were available for analysis. The behavior of the  $X$  and  $Y$  correlation functions and lengths with  $\theta_{BV}$  are consistent with an energy dominant 2D turbulence. At  $\theta_{BV} < 30^\circ$ , few intervals were found, and high-energy proton data showed that there was often a magnetic field connection with the bow shock. No energetic protons were found for larger  $\theta_{BV}$  in the vast majority of the data analyzed.

While this study has provided valuable insights into solar wind turbulence at dissipation scales, its reliance on single-spacecraft data imposed significant limitations, particularly in resolving fluctuations at small angles relative to the mean magnetic field. The modified correlation function analysis used proved effective within these constraints, but lacked the spatial resolution required to fully capture the three-dimensional (3D) structure of turbulence.

We hypothesize that applying this modified correlation function analysis in conjunction with multi-spacecraft observations (i.e. MMS 2, 3, and 4), would address these limitations by enabling the sampling of the full 3D turbulent structure—without resorting to times of radial magnetic field when the data is contaminated by waves excited by upstream particles. Such an approach would provide a more complete characterization of the turbulent anisotropy and nature of wave-particle interactions in the solar wind.

## Conflict of Interest

The authors declare no conflicts of interest relevant to this study.

## Data Availability Statement

Data for this research were obtained from the Magnetospheric Multiscale Mission (MMS) via the MMS Science Data Center, managed by the Laboratory for Atmospheric and Space Physics (LASP) (Burch et al., 2016). Complementary data for this investigation was obtained from the Advanced Composition Explorer (ACE) spacecraft (Chiu et al., 1998; McComas et al., 1998; Smith et al., 1998). Data analysis was conducted using the Python-based Space Physics Environment Data Analysis System (PySPEDAS) (Grimes et al., 2022). Spacecraft orbit and Earth's bow shock visualizations were generated with 3DView, a scientific visualization tool developed by Centre National D'études Spatiales (CNES), which supports spacecraft positioning, planetary ephemerides, and representations of observational, simulated, and modeled data (Génot et al., 2018).

## Acknowledgments

This MMS-EPD work supported by MMS Prime Contract NASA499879Q. CWS is supported under UNH subcontract from SwRI under NASA Contract NNG04EB99C as well as Contract 149961 from JHU/APL in support of the MMS program. BJV is supported under UNH subcontract from SwRI under NASA Contract NNG04EB99C. SR acknowledges funding from the MMS Early Career Award 80NSSC25K7353.

## References

- Abbo, L., Ofman, L., Antiochos, S. K., Hansteen, V. H., Harra, L., Ko, Y.-K., et al. (2016). Slow solar wind: Observations and modeling. *Space Science Reviews*, 201(1), 55–108. <https://doi.org/10.1007/s11214-016-0264-1>
- Alexandrova, O., Chen, C. H. K., Sorriso-Valvo, L., Horbury, T. S., & Bale, S. D. (2013). Solar wind turbulence and the role of ion instabilities. *Space Science Reviews*, 178(2), 101–139. <https://doi.org/10.1007/s11214-013-0004-8>
- Barnes, A. (1966). Collisionless damping of hydromagnetic waves. *The Physics of Fluids*, 9(8), 1483–1495. <https://doi.org/10.1063/1.1761882>
- Barnes, A. (1979). Hydromagnetic waves and turbulence in the solar wind. *Solar System Plasma Physics*, 1, 249–319.
- Belcher, J. W., & Davis, L., Jr. (1971). Large-amplitude Alfvén waves in the interplanetary medium, 2. *Journal of Geophysical Research* (1896–1977), 76(16), 3534–3563. <https://doi.org/10.1029/JA076i016p03534>
- Bieber, J. W., Wanner, W., & Matthaeus, W. H. (1996). Dominant two-dimensional solar wind turbulence with implications for cosmic ray transport. *Journal of Geophysical Research*, 101(A2), 2511–2522. <https://doi.org/10.1029/95JA02588>
- Bourouaine, S., & Chandran, B. D. G. (2013). Observational test of stochastic heating in low- $\beta$  fast-solar-wind streams. *The Astrophysical Journal*, 774(2), 96. <https://doi.org/10.1088/0004-637X/774/2/96>
- Bowen, T. A., Bale, S. D., Chandran, B. D. G., Chasapis, A., Chen, C. H. K., Dudok de Wit, T., et al. (2024). Mediation of collisionless turbulent dissipation through cyclotron resonance. *Nature Astronomy*, 8(4), 482–490. <https://doi.org/10.1038/s41550-023-02186-4>
- Burch, J. L., Moore, T. E., Torbert, R. B., & Giles, B. L. (2016). Magnetospheric multiscale overview and science objectives. *Space Science Reviews*, 199(1), 5–21. <https://doi.org/10.1007/s11214-015-0164-9>
- Chiu, M., Von-Mehlem, U., Willey, C., Betenbaugh, T., Maynard, J., Krein, J., et al. (1998). ACE spacecraft. *Space Science Reviews*, 86(1), 257–284. <https://doi.org/10.1023/A:1005002013459>



- Cho, J., & Vishniac, E. T. (2000). The anisotropy of Magnetohydrodynamic Alfvénic turbulence. *The Astrophysical Journal*, 539(1), 273–282. <https://doi.org/10.1086/309213>
- Coleman, P. J. (1966). Hydromagnetic waves in the interplanetary plasma. *Physical Review Letters*, 17(4), 207–211. <https://doi.org/10.1103/PhysRevLett.17.207>
- D'Amicis, R., & Bruno, R. (2015). On the origin of highly Alfvénic slow solar wind. *The Astrophysical Journal*, 805(1), 84. <https://doi.org/10.1088/0004-637X/805/1/84>
- Dasso, S., Milano, L. J., Matthaeus, W. H., & Smith, C. W. (2005). Anisotropy in fast and slow solar wind fluctuations. *The Astrophysical Journal*, 635(2), L181–L184. <https://doi.org/10.1086/499559>
- Davis, N., Chandran, B. D. G., Bowen, T. A., Badman, S. T., de Wit, T. D., Chen, C. H. K., et al. (2023). The evolution of the 1/f range within a single fast-solar-wind stream between 17.4 and 45.7 solar radii. *The Astrophysical Journal*, 950(2), 154. <https://doi.org/10.3847/1538-4357/a1cd177>
- Dmitruk, P., Matthaeus, W. H., & Seenu, N. (2004). Test particle energization by current sheets and nonuniform fields in magnetohydrodynamic turbulence. *The Astrophysical Journal*, 617(1), 667–679. <https://doi.org/10.1086/425301>
- Duan, D., Bowen, T. A., Chen, C. H. K., Mallet, A., He, J., Bale, S. D., et al. (2020). The radial dependence of proton-scale magnetic spectral break in slow solar wind during PSP encounter 2. *The Astrophysical Journal—Supplement Series*, 246(2), 55. <https://doi.org/10.3847/1538-4365/a1b672d>
- Fairfield, D. H. (1971). Average and unusual locations of the Earth's magnetopause and bow shock. *Journal of Geophysical Research* (1896–1977), 76(28), 6700–6716. <https://doi.org/10.1029/JA076i028p06700>
- Génot, V., Beigbeder, L., Popescu, D., Dufour, N., Gangloff, M., Bouchemit, M., et al. (2018). Science data visualization in planetary and heliospheric contexts with 3DView. *Planetary and Space Science*, 150, 111–130. <https://doi.org/10.1016/j.pss.2017.07.007>
- Gershman, D. J., Giles, B. L., Pollock, C. J., Moore, T. E., Kreisler, S., & Burch, J. L. (2022). Mms 1 Fast Plasma Investigation, Dual Electron Spectrometer (FPI, DES) distribution moments, Level 2 (L2), burst mode, 30 Ms data. *NASA Space Physics Data Facility*. <https://doi.org/10.48322/6172-ZW20>
- Goldstein, M. L., Roberts, D. A., & Matthaeus, W. H. (1995). Magnetohydrodynamic turbulence in the solar wind. *Annual Review of Astronomy and Astrophysics*, 33(33), 283–325. <https://doi.org/10.1146/annurev.aa.33.090195.001435>
- Grimes, E. W., Harter, B., Hatzigeorgiu, N., Drozdov, A., Lewis, J. W., Angelopoulos, V., et al. (2022). The space physics environment data analysis system in python. *Frontiers in Astronomy and Space Sciences*, 9, 1020815. <https://doi.org/10.3389/fspas.2022.1020815>
- Hamilton, K., Smith, C. W., Vasquez, B. J., & Leamon, R. J. (2008). Anisotropies and helicities in the solar wind inertial and dissipation ranges at 1 AU. *Journal of Geophysical Research: Space Physics*, 113(A1). <https://doi.org/10.1029/2007JA012559>
- Hollweg, J. V., & Isenberg, P. A. (2002). Generation of the fast solar wind: A review with emphasis on the resonant cyclotron interaction. *Journal of Geophysical Research*, 107(A7), SSH12–1–SSH12–37. <https://doi.org/10.1029/2001JA000270>
- Isenberg, P. A., & Vasquez, B. J. (2015). Kinetic evolution of coronal hole protons by imbalanced ion-cyclotron waves: Implications for measurements by solar probe plus. *The Astrophysical Journal*, 808(2), 119. <https://doi.org/10.1088/0004-637X/808/2/119>
- Kilpua, E. K. J., Madjarska, M. S., Karna, N., Wiegmann, T., Farrugia, C., Yu, W., & Andreeva, K. (2016). Sources of the slow solar wind during the solar cycle 23/24 minimum. *Solar Physics*, 291(8), 2441–2456. <https://doi.org/10.1007/s11207-016-0979-x>
- Leamon, R. J., Smith, C. W., Ness, N. F., Matthaeus, W. H., & Wong, H. K. (1998). Observational constraints on the dynamics of the interplanetary magnetic field dissipation range. *Journal of Geophysical Research*, 103(A3), 4775–4787. <https://doi.org/10.1029/97JA03394>
- Leamon, R. J., Smith, C. W., Ness, N. F., & Wong, H. K. (1999). Dissipation range dynamics: Kinetic Alfvén waves and the importance of  $\beta$  e. *Journal of Geophysical Research*, 104(A10), 22331–22344. <https://doi.org/10.1029/1999JA900158>
- Magyar, N., & Doorselaere, T. V. (2022). Phase mixing and the 1/f spectrum in the solar wind. *The Astrophysical Journal*, 938(2), 98. <https://doi.org/10.3847/1538-4357/ac8b81>
- Markovskii, S. A., & Vasquez, B. J. (2011). A short-timescale channel of dissipation of the strong solar wind turbulence. *The Astrophysical Journal*, 739(1), 22. <https://doi.org/10.1088/0004-637X/739/1/22>
- Marsch, E., Mühlhäuser, K.-H., Rosenbauer, H., Schwenn, R., & Denskat, K. U. (1981). Pronounced proton core temperature anisotropy, ion differential speed, and simultaneous Alfvén wave activity in slow solar wind at 0.3 AU. *Journal of Geophysical Research*, 86(A11), 9199–9203. <https://doi.org/10.1029/JA086iA11p09199>
- Matthaeus, W. H., Ghosh, S., Oughton, S., & Roberts, D. A. (1996). Anisotropic three-dimensional MHD turbulence. *Journal of Geophysical Research*, 101(A4), 7619–7629. <https://doi.org/10.1029/95JA03830>
- Matthaeus, W. H., & Goldstein, M. L. (1982). Measurement of the rugged invariants of magnetohydrodynamic turbulence in the solar wind. *Journal of Geophysical Research*, 87(A8), 6011–6028. <https://doi.org/10.1029/JA087iA08p06011>
- Matthaeus, W. H., & Goldstein, M. L. (1986). Low-Frequency  $\delta B^2$  Noise in the Interplanetary Magnetic Field. *Physical Review Letters*, 57(4), 495–498. <https://doi.org/10.1103/PhysRevLett.57.495>
- Matthaeus, W. H., Goldstein, M. L., & Roberts, D. A. (1990). Evidence for the presence of quasi-two-dimensional nearly incompressible fluctuations in the solar wind. *Journal of Geophysical Research*, 95(A12), 20673–20683. <https://doi.org/10.1029/JA095iA12p20673>
- Matthaeus, W. H., Oughton, S., Ghosh, S., & Hossain, M. (1998). Scaling of anisotropy in hydromagnetic turbulence. *Physical Review Letters*, 81(10), 2056–2059. <https://doi.org/10.1103/PhysRevLett.81.2056>
- Matthaeus, W. H., Oughton, S., Pontius, D. H., Jr., & Zhou, Y. (1994). Evolution of energy-containing turbulent eddies in the solar wind. *Journal of Geophysical Research*, 99(A10), 19267–19287. <https://doi.org/10.1029/94JA01233>
- Mauk, B. H., Blake, J. B., Baker, D. N., Clemmons, J. H., Reeves, G. D., Spence, H. E., et al. (2016). The Energetic Particle Detector (EPD) investigation and the Energetic Ion Spectrometer (EIS) for the Magnetospheric Multiscale (MMS) mission. *Space Science Reviews*, 199(1), 471–514. <https://doi.org/10.1007/s11214-014-0055-5>
- McComas, D. J., Bame, S. J., Barker, P., Feldman, W. C., Phillips, J. L., Riley, P., & Griffée, J. W. (1998). Solar Wind Electron Proton Alpha Monitor (SWEPAM) for the advanced composition explorer. In C. T. Russell, R. A. Mewaldt, & T. T. Von Rosenvinge (Eds.), *The advanced composition explorer mission* (pp. 563–612). Springer Netherlands. [https://doi.org/10.1007/978-94-011-4762-0\\_20](https://doi.org/10.1007/978-94-011-4762-0_20)
- Oughton, S., Priest, E. R., & Matthaeus, W. H. (1994). The influence of a mean magnetic field on three-dimensional magnetohydrodynamic turbulence. *Journal of Fluid Mechanics*, 280, 95–117. <https://doi.org/10.1017/S0022112094002867>
- Paschmann, G., Haerendel, G., Scokpe, N., Möbius, E., Lühr, H., & Carlson, C. W. (1988). Three-dimensional plasma structures with anomalous flow directions near the Earth's bow shock. *Journal of Geophysical Research*, 93(A10), 11279–11294. <https://doi.org/10.1029/JA093iA10p11279>
- Peebles, P. J. E. (1968). Recombination of the primeval plasma. *The Astrophysical Journal*, 153, 1. <https://doi.org/10.1086/149628>
- Podesta, J. J., Roberts, D. A., & Goldstein, M. L. (2006). Self-similar scaling of magnetic energy in the inertial range of solar wind turbulence. *Journal of Geophysical Research: Space Physics*, 111(A9). <https://doi.org/10.1029/2006JA011766>

- Pollock, C., Moore, T., Jacques, A., Burch, J., Gliese, U., Saito, Y., et al. (2016). Fast plasma investigation for Magnetospheric multiscale. *Space Science Reviews*, 199(1), 331–406. <https://doi.org/10.1007/s11214-016-0245-4>
- Roberts, O. W., Nakamura, R., Coffey, V. N., Gershman, D. J., Volwerk, M., Varsani, A., et al. (2021). A study of the solar wind ion and electron measurements from the magnetospheric multiscale mission's fast plasma investigation. *Journal of Geophysical Research: Space Physics*, 126(10), e2021JA029784. <https://doi.org/10.1029/2021JA029784>
- Russell, C. T., Anderson, B. J., Baumjohann, W., Bromund, K. R., Dearborn, D., Fischer, D., et al. (2016). The magnetospheric multiscale magnetometers. *Space Science Reviews*, 199(1), 189–256. <https://doi.org/10.1007/s11214-014-0057-3>
- Russell, C. T., Magnes, W., Wei, H., Bromund, K. R., Plaschke, F., Fischer, D., et al. (2022). Mms 1 Flux Gate Magnetometer (FGM) dc magnetic field, Level 2 (L2), survey mode, 8 or 16 sample/s, v4/5 data. *NASA Space Physics Data Facility*. <https://doi.org/10.48322/MXBX-R466>
- Sahraoui, F., Huang, S. Y., Belmont, G., Goldstein, M. L., Rétnino, A., Robert, P., & De Patoul, J. (2013). Scaling of the electron dissipation range of solar wind turbulence. *The Astrophysical Journal*, 777(1), 15. <https://doi.org/10.1088/0004-637X/777/1/15>
- Schwartz, S. J. (1995). Hot flow anomalies near the Earth's bow shock. *Advances in Space Research*, 15(8), 107–116. [https://doi.org/10.1016/0273-1177\(94\)00092-F](https://doi.org/10.1016/0273-1177(94)00092-F)
- Shebalin, J. V., Matthaeus, W. H., & Montgomery, D. (1983). Anisotropy in MHD turbulence due to a mean magnetic field. *Journal of Plasma Physics*, 29(3), 525–547. <https://doi.org/10.1017/S0022377800000933>
- Smith, C. W., Hamilton, K., Vasquez, B. J., & Leamon, R. J. (2006). Dependence of the dissipation range spectrum of interplanetary magnetic fluctuations on the rate of energy cascade. *The Astrophysical Journal*, 645(1), L85–L88. <https://doi.org/10.1086/506151>
- Smith, C. W., L'Heureux, J., Ness, N. F., Acuña, M. H., Burlaga, L. F., & Scheifele, J. (1998). The ace magnetic fields experiment. In C. T. Russell, R. A. Mewaldt, & T. T. Von Rosenvinge (Eds.), *The advanced composition explorer mission* (pp. 613–632). Springer Netherlands. [https://doi.org/10.1007/978-94-011-4762-0\\_21](https://doi.org/10.1007/978-94-011-4762-0_21)
- Smith, C. W., & Vasquez, B. J. (2021). Driving and dissipation of solar-wind turbulence: What is the evidence? *Frontiers in Astronomy and Space Sciences*, 7, 611909. <https://doi.org/10.3389/fspas.2020.611909>
- Smith, C. W., & Vasquez, B. J. (2024). The unsolved problem of solar-wind turbulence. *Frontiers in Astronomy and Space Sciences*, 11, 1371058. <https://doi.org/10.3389/fspas.2024.1371058>
- Smith, C. W., Vasquez, B. J., & Hollweg, J. V. (2012). Observational constraints on the role of cyclotron damping and kinetic Alfvén waves in the solar wind. *The Astrophysical Journal*, 745(1), 8. <https://doi.org/10.1088/0004-637X/745/1/8>
- Smith, C. W., Vasquez, B. J., & Stenkowski, M. R. (2013). Analysis of multi-dimensional correlation functions in the solar wind. In *Solar wind 13* (Vol. 1539, pp. 271–274). AIP. <https://doi.org/10.1063/1.4811040>
- Svalgaard, L., & Wilcox, J. M. (1974). The spiral interplanetary magnetic field: A polarity and sunspot cycle variation. *Science*, 186(4158), 51–53. <https://doi.org/10.1126/science.186.4158.51>
- Taylor, G. I. (1938). The spectrum of turbulence. *Proceedings of the Royal Society of London. Series A—Mathematical and Physical Sciences*, 164(919), 476–490. <https://doi.org/10.1098/rspa.1938.0032>
- TenBarge, J. M., Howes, G. G., & Dorland, W. (2013). Collisionless damping at electron scales in solar wind turbulence. *The Astrophysical Journal*, 774(2), 139. <https://doi.org/10.1088/0004-637X/774/2/139>
- Thomas, V. A., Winske, D., Thomsen, M. F., & Onsager, T. G. (1991). Hybrid simulation of the formation of a hot flow anomaly. *Journal of Geophysical Research*, 96(A7), 11625–11632. <https://doi.org/10.1029/91JA01092>
- Tooley, C. R., Black, R. K., Robertson, B. P., Stone, J. M., Pope, S. E., & Davis, G. T. (2016). The magnetospheric multiscale constellation. *Space Science Reviews*, 199(1), 23–76. <https://doi.org/10.1007/s11214-015-0220-5>
- Torbert, R. B., Russell, C. T., Magnes, W., Ergun, R. E., Lindqvist, P.-A., LeContel, O., et al. (2016). The FIELDS instrument suite on MMS: Scientific objectives, measurements, and data products. *Space Science Reviews*, 199(1), 105–135. <https://doi.org/10.1007/s11214-014-0109-8>
- Vasquez, B. J. (2015). Heating rate scaling of turbulence in the proton kinetic regime. *The Astrophysical Journal*, 806(1), 33. <https://doi.org/10.1088/0004-637X/806/1/33>
- Vasquez, B. J., Markovskii, S. A., & Chandran, B. D. G. (2014). Three-dimensional hybrid simulation study of anisotropic turbulence in the proton kinetic regime. *The Astrophysical Journal*, 788(2), 178. <https://doi.org/10.1088/0004-637X/788/2/178>
- Verscharen, D., Klein, K. G., & Maruca, B. A. (2019). The multi-scale nature of the solar wind. *Living Reviews in Solar Physics*, 16(1), 5. <https://doi.org/10.1007/s41116-019-0021-0>
- Weygand, J. M., Matthaeus, W. H., Dasso, S., Kivelson, M. G., Kistler, L. M., & Moukikis, C. (2009). Anisotropy of the Taylor scale and the correlation scale in plasma sheet and solar wind magnetic field fluctuations. *Journal of Geophysical Research: Space Physics*, 114(A7). <https://doi.org/10.1029/2008JA013766>
- Yang, Y., Matthaeus, W. H., Parashar, T. N., Haggerty, C. C., Roytershteyn, V., Daughton, W., et al. (2017). Energy transfer, pressure tensor, and heating of kinetic plasma. *Physics of Plasmas*, 24(7), 072306. <https://doi.org/10.1063/1.4990421>